

Wave Height Mapping From HF Radar-Measured Surface Current Data Based on a Cascaded LSTM Network

Yingwei Tian¹, Member, IEEE, Xinyi Ma¹, Jing Yang¹, Member, IEEE, Caijun Wang¹, and Xujing Yan

Abstract—High-frequency (HF) surface wave radar has been widely used for measuring sea surface current, but its accuracy and spatial coverage of sea wave measurement are limited. A wave height mapping method based on HF radar-measured surface currents is proposed in this article. The tidal currents are first estimated and subtracted from the radar-measured surface currents, and then the geostrophic currents are removed. The remaining currents, along with the wind directions, are used as input data to a cascaded long short-term memory network. This network contains two stages. The first stage divides the input data into two groups of high and low sea states, and the second stage performs wave height inversion for each group separately. By combining the inversion results of the two groups, wave height maps are obtained. The algorithm is verified using the experimental data from the southwestern Taiwan Strait. Using the numerical wave height fields as the ground truth, the proposed algorithm has a root-mean-square error of 0.35 m and a correlation coefficient of 0.90.

Index Terms—High-frequency (HF) radar, long short-term memory (LSTM) network, surface current, wave height map, wind direction.

I. INTRODUCTION

ACCURATE measurement of coastal wave height is crucial for maritime safety, coastal engineering, climate and weather studies, environmental monitoring, and wave energy resource assessment. High-frequency (HF) surface wave radar enables all-weather, real-time, and continuous monitoring of sea surface without the need for physical instruments in the water, making it a powerful tool for measuring sea wave height.

In 1977, according to the first-order [1] and second-order [2] sea surface scattering theory, Barrick [3] proposed a wave

height inversion algorithm for HF radar which is based on the integral ratio of the second-order continuum spectrum to the first-order spectrum. Since then, many scholars have worked on simplifying and optimizing this algorithm [4], [5], [6]. Besides, since the wave height can be easily calculated from the ocean wave spectrum, much effort has been put into inversion of the wave spectrum from the second-order continuum spectrum of HF radar [7], [8], [9], [10], [11]. To obtain the wave height map using these methods, beamforming is usually required to resolve the second-order scattering echoes from different azimuths, which is not applicable to the compact HF radar due to its broad beam width. In addition, the accuracy of wave height inversion is vulnerable to the signal-to-noise ratio (SNR) of the second-order continuum spectrum, which is usually low in low sea state and long distance situations [12]. Moreover, due to the wide frequency range occupied by the second-order continuum spectrum, vessel echoes and radio communication signals tend to interfere with the inversion accuracy [13].

In order to solve the above-mentioned problems, a wave height inversion algorithm based on the power of first-order Bragg peaks [14] is proposed. Because of the relatively high power of first-order peaks, this method significantly increases the measurement distance and makes it possible to distinguish the echo azimuths by the direction-finding algorithm [15], thus allowing the wave height map to be obtained. However, this method is not suitable for high sea state, as the Bragg waves are usually saturated in this case. In addition, the inversion performance is influenced by the wave directional spreading [16].

The wave height inversion method based on the power ratio of the second-order harmonic peak (SHP) over the first-order peak [17], [18], [19] provides a solution to the inapplicability problem in high sea state. The accuracy of this method is limited by the SNR of SHP, so its accuracy and coverage of wave height estimation in low sea state are challenging.

Inverting wave height from the power ratio of the first-order peaks associated with two radar frequencies [20], [21] can address the directional spreading problem, but it is not suitable for short-distance application because the power ratio is not sensitive to wave height variation in this case [22].

In summary, the existing HF radar wave height inversion algorithms still have many challenges in terms of spatial coverage, accuracy, and measurable wave height range. Some researchers [23], [24] have attempted to use a neural

Manuscript received 10 January 2024; revised 15 March 2024 and 24 April 2024; accepted 21 May 2024. Date of publication 28 May 2024; date of current version 13 September 2024. This work was supported in part by the National Key R&D Program of China under Grant 2022YFC2806300, in part by the National Natural Science Foundation of China under Grant 62071337, in part by the Natural Science Foundation of Hubei Province under Grant 2022CFB055, and in part by Guangdong Basic and Applied Basic Research Foundation under Grant 2024A1515011961. (Corresponding authors: Jing Yang; Caijun Wang.)

Yingwei Tian is with the School of Electronic Information, Wuhan University, Wuhan 430072, China, and also with the Wuhan University Shenzhen Research Institute, Shenzhen 518057, China (e-mail: tianyw@whu.edu.cn).

Xinyi Ma, Jing Yang, Caijun Wang, and Xujing Yan are with the School of Electronic Information, Wuhan University, Wuhan 430072, China (e-mail: 2018302120033@whu.edu.cn; janyang628@whu.edu.cn; wcj@whu.edu.cn; 2021282120178@whu.edu.cn).

Digital Object Identifier 10.1109/JSTARS.2024.3406023

network-based approach to invert wave height by combining multiple Doppler spectral features as described previously, but the improvements are limited.

In contrast, the surface current measurement capability of HF radar has been widely recognized and applied [25], [26], [27]. Both the Ekman and Stokes components of surface current are closely related to wave height. Thus, based on the surface currents estimated by HF radar, a new wave height mapping algorithm is proposed in this article. Initially, the tidal and geostrophic components are estimated and removed from the surface current and the remaining current is defined as the ageostrophic residual current (ARC). Then, the wind direction is extracted from the ratio of the positive frequency first-order spectra to the negative one. Furthermore, a cascaded long short-term memory (LSTM) network, which is composed of two stages, is proposed to invert the wave height map from the ARCs and wind directions. The first-stage divides the input data into two groups of high and low sea states, and the second-stage performs wave height inversion on each group separately. The final wave height maps are generated after combining the inversion results of the two groups.

The rest of the article is organized as follows. Section II presents the theoretical background of the wave height inversion algorithm. Section III details the inversion method. The retrieval results of a field experiment and the discussion are given in Section IV. Finally, Section V concludes this article.

II. THEORETICAL BACKGROUND

The sea surface current \vec{U} measured by HF radar can be expressed as the sum of wind-induced current \vec{U}_w , wave-induced current \vec{U}_s , tidal current \vec{U}_t , and geostrophic current \vec{U}_g [28], [29]

$$\vec{U} = \vec{U}_w + \vec{U}_s + \vec{U}_t + \vec{U}_g. \quad (1)$$

Among these components, the ones most closely related to wave height are \vec{U}_w and \vec{U}_s , which are governed by Ekman theory and Stokes mass transport theory, respectively.

A. Wind-Induced Current

A classical view of the wind-induced current is Ekman's solution of a momentum balance between the wind stress and Coriolis force [30]. Under the assumption of a steady, homogeneous, horizontal flow with friction on a rotating Earth and constant vertical eddy viscosity, the Ekman drift model can be expressed as

$$\vec{U}_w = \frac{\vec{\tau} e^{-i\pi/4}}{\rho_w \sqrt{f} A_z} \frac{\sinh \left[(1+i)(h-z) \sqrt{f/(2A_z)} \right]}{\cosh \left[(1+i)h \sqrt{f/(2A_z)} \right]} \quad (2)$$

where $\vec{\tau}$ is the wind shear stress, i is imaginary unit, ρ_w is the water density, $f = 2\omega_E \sin \varphi$ is the Coriolis parameter, ω_E is the angular velocity of Earth, φ is the latitude, A_z is the vertical eddy viscosity in the water, h is the undisturbed water depth, z is the vertical distance between the observation point and the sea surface. The value of A_z cannot be obtained theoretically and is generally calculated from experimental observations.

The wind shear stress $\vec{\tau}$ can be written as [29]

$$\vec{\tau} = \rho_a C_D V_{10} \vec{V}_{10} \quad (3)$$

where ρ_a is the air density, C_D is the drag coefficient whose value is related to the wind speed [31], and \vec{V}_{10} is the wind vector at a height of 10 m above the sea surface.

Equations (2) and (3) suggest a quadratic relation between the wind-induced current speed and the wind speed. However, since A_z and C_D are not constants in practice, the real relationship is more complicated.

When wind blows over the ocean surface, it transfers energy to the water, causing not only currents but also waves. Many studies have been done to obtain the wind wave spectrum, or the relationship between wind and statistical characteristics of waves, such as the wave height. One of the most widely applied formulas was proposed by Sverdrup and Munk and later revised by Bretschneider (SMB equation), which can be written as [32]

$$\frac{gH_s}{V_{10}^2} = 0.26 \tanh \left[\frac{1}{10^2} \left(\frac{gF}{V_{10}^2} \right)^{1/2} \right] \quad (4)$$

where g is the gravitational acceleration, H_s is the significant wave height, and F is the wind fetch.

Another well-known formula is based on the JONSWAP wave spectrum [32]

$$\frac{gH_s}{V_{10}^2} = 1.6 \times 10^{-3} \left(\frac{gF}{V_{10}^2} \right)^{1/2}. \quad (5)$$

It can be concluded from (2), (4), and (5) that wind is the main factor of both wind-induced current and wave height, so the wind-induced current and wave height should be numerically correlated.

B. Wave-Induced Current

In addition to winds, surface gravity waves also affect surface currents through wave-induced currents and wave-current interactions [33].

The wave-induced current component, i.e., the Stokes drift \vec{U}_s , can be estimated from wave energy spectrum distribution $E(\Omega, \theta)$ as the following [34]:

$$\vec{U}_s = \frac{2}{g} \int_0^{2\pi} \int_0^\infty \Omega^3 \hat{\kappa} e^{-2\kappa z} E(\Omega, \theta) d\Omega d\theta \quad (6)$$

where Ω is the sea wave radian frequency, θ is the sea wave propagation direction, κ is the magnitude of wavenumber vector, and $\hat{\kappa}$ is the unit vector in the wave propagation direction.

The significant wave height can also be estimated from the wave energy spectrum using the following equation [32]:

$$H_s \approx 4 \sqrt{\int_0^{2\pi} \int_0^\infty E(\Omega, \theta) d\Omega d\theta}. \quad (7)$$

Equations (6) and (7) suggest that the Stokes drift and the significant wave height can be linked by the wave energy spectrum.

In addition to Stokes drift, waves also affect the acceleration of surface currents by momentum fluxes from the atmosphere. During wave growth, the momentum flux from winds that goes

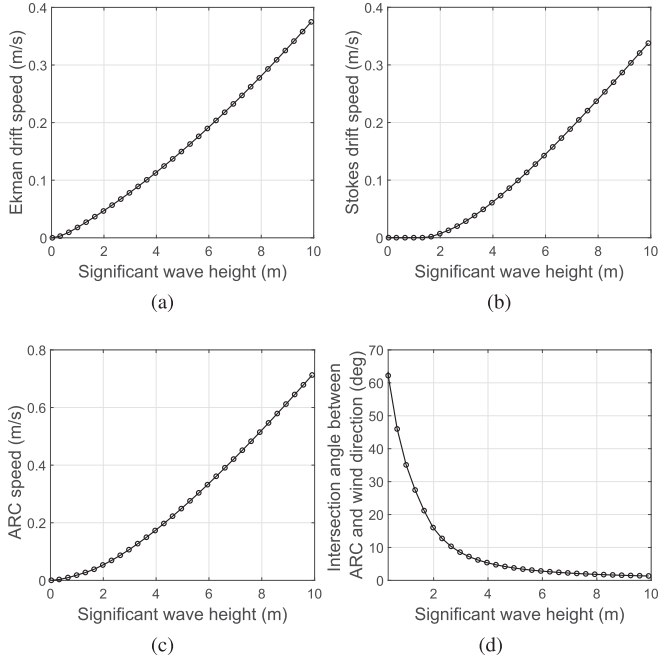


Fig. 1. Simulated current speed and direction at 1.9 m depth for different wave heights. (a) Ekman drift speed. (b) Stokes drift speed. (c) ARC speed. (d) Intersection angle between ARC and wind direction.

into currents is reduced by 10% – 30% since a portion of the flux enters the wave field. After the waves have traveled a long distance and time, they release their momentum to the surface currents through wave breaking [33]. Moreover, wave–current interactions result in small-scale surface current patterns, such as Langmuir circulation cells [35] and rip currents [36].

C. Numerical Simulation

In order to further observe the relationship between surface current and wave height, Fig. 1 presents the simulation results based on (2) and (6). Fig. 1(a) and (b) shows the variation of Ekman drift speed and Stokes drift speed with significant wave height, respectively. Fig. 1(c) and (d) demonstrates how the speed and direction of the sum of the Ekman drift and Stokes drift vary with the significant wave height, respectively. In this article, we define the sum of the two currents as ARC \vec{U}_a

$$\vec{U}_a = \vec{U}_w + \vec{U}_s. \quad (8)$$

Since the experimental data used in Section IV of this article are provided by an HF radar operated at 13 MHz, which measures current at a depth of 1.9 m below the sea surface [37], z is set to 1.9 m in the simulation. The undisturbed water depth h is set to 27 m. A_z is set as a linear function of depth $A_z = 0.4z\sqrt{|\vec{\tau}|/\rho_w}$ [38]. The JONSWAP wave spectrum [39] is adopted and the wind fetch F is set to 400 km. The mean wave direction is assumed to be consistent with the wind direction.

Fig. 1 illustrates that with the increase of significant wave height, the velocities of both Ekman and Stokes drifts increase, with the latter increasing slowly at significant wave heights lower than 2 m. As wave height increases, the speed of the ARC

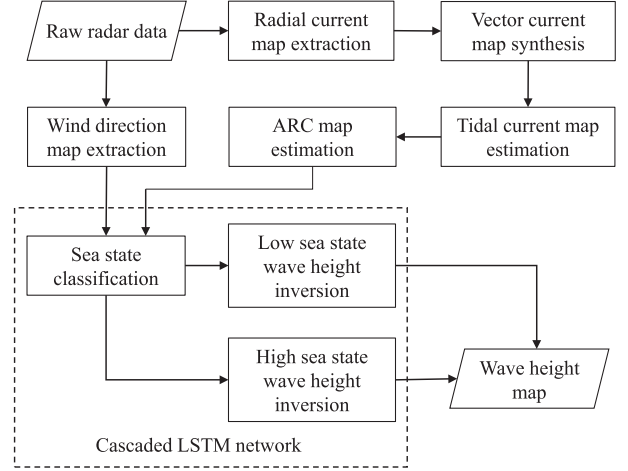


Fig. 2. Procedure of wave height map inversion.

increases and its direction turns closer to the wind direction. Apparently it is promising to invert wave height from the ARC due to the strong correlation between them.

However, it is not suitable to calculate the wave height directly from the ARC, first, because the existing analytical expressions are not accurate enough due to the ignorance of many complex wave–current interaction mechanisms, and second, because some parameters in the analytical expressions are difficult to determine, such as the wind fetch and the wave energy spectrum. Therefore, a deep learning-based approach is proposed in this article.

III. WAVE HEIGHT INVERSION METHOD

A. Algorithm Steps

Fig. 2 shows the steps of the wave height map inversion algorithm proposed in this article.

Step 1: The radial current map is extracted from the raw radar data.

When grazing-incidence HF electromagnetic waves illuminate the sea surface, those sea waves propagating along the radial direction with wavelengths half the wavelengths of the electromagnetic waves generate Bragg scattering. In this case, waves moving toward the radar produce first-order Bragg peaks with positive frequencies in the Doppler spectrum of radar echoes, and waves moving away from the radar produce negative frequency first-order peaks. The power of the first-order peaks is proportional to the first-order backscattering cross-section of HF radar which is given by [1]

$$\sigma_1(\omega) = 2^6 \pi k^4 \sum_{m=\pm 1} E(-2m\vec{k}) \delta(\omega - m\omega_B + 2\vec{k} \cdot \vec{v}_c) \quad (9)$$

where ω is the angular frequency of radio waves, \vec{k} is the wave number vector of radio waves, and k is its magnitude. ω_B is the angular frequency of Bragg waves, $\delta(\cdot)$ is Dirac function, and \vec{v}_c is the surface current. It can be seen that the surface current can cause the shift of the first-order peaks relative to the Bragg

frequency, i.e.,

$$\Delta\omega = 2\vec{k} \cdot \vec{v}_c = 2kv_r \quad (10)$$

where v_r is the radial component of surface current. Thus, the radial surface current can be calculated from the offset of first-order peaks.

During extraction of the radial current map, the range cell separation is achieved through pulse compression of the echoes, and the specific steps include frequency mixing the echoes with the transmitted frequency modulated interrupted continuous wave (FMICW) signal, low-pass filtering and Fourier transforming. The azimuth information is extracted using the digital beamforming technique or the multiple signal classification algorithm [15].

Step 2: The vector current map is synthesized using the radial current maps from two or more HF radars.

Step 3: The tidal current map is estimated from the vector current map with the method detailed in Section III-B.

Step 4: The geostrophic current is estimated and the ARC map is calculated using the following equation, which is derived from (1) and (8):

$$\vec{U}_a = \vec{U} - \vec{U}_t - \vec{U}_g. \quad (11)$$

Step 5: The wind direction map is extracted from the raw radar data.

In (9), if the ocean wave spectrum $E(\vec{\kappa})$ is expressed for simplicity as a product of the omnidirectional ocean wave spectrum $E(\kappa)$ and the wave directional spreading function $G(\theta)$ [40], [41], [42] as follows:

$$E(\vec{\kappa}) = E(\kappa)G(\theta) \quad (12)$$

then the power ratio of the positive frequency first-order peak to the negative frequency one is

$$R = \frac{E(-2\vec{k})}{E(2\vec{k})} = \frac{G(\pi + \theta_r - \theta_w)}{G(\theta_r - \theta_w)} \quad (13)$$

where θ_r is the direction where the radar beam is pointing and θ_w is the mean direction of sea waves with wavenumber $2k$. It can be seen that if θ_w is assumed to be the same as the wind direction, then the wind direction can be calculated from R .

Step 6: The wave height map is obtained by substituting the wind direction map and the ARC map into the cascaded LSTM network.

B. Tidal Current Extraction

Tidal currents are highly periodic, whereas other current components are generally not. Using this feature, it is easy to separate the tidal currents from the total ocean currents. The most commonly used method is harmonic analysis [43].

The time series of vector current in each space cell $U(t)$ can be decomposed into the eastward component $u(t)$ and the northward component $v(t)$

$$U(t) = u(t) + iv(t). \quad (14)$$

Since the tidal current can be represented by the sum of a series of harmonic constituents, the two components of vector

current can be denoted as

$$\begin{cases} u(t) = u_0(t) + \sum_j u_j \cos(\sigma_j t - \xi_j) \\ v(t) = v_0(t) + \sum_j v_j \cos(\sigma_j t - \eta_j) \end{cases} \quad (15)$$

where $u_0(t)$ and $v_0(t)$ are the two orthogonal residual current components. Residual current means the remaining portion of the vector current after removing the tidal current. $\sum_j u_j \cos(\sigma_j t - \xi_j)$ and $\sum_j v_j \cos(\sigma_j t - \eta_j)$ denote the two orthogonal tidal current components. u_j , ξ_j , v_j , and η_j are the harmonic constants at the frequency σ_j , which are usually calculated using the least squares method. In this article, an open source MATLAB toolbox T_Tide [44] is used for the harmonic tidal analysis, and the harmonic analysis and residual current calculation are performed separately for each space cell.

C. Geostrophic Current Estimation

Geostrophic current is a steady flow when the horizontal pressure gradient force is in equilibrium with the Coriolis force, without considering the effect of sea surface winds and the friction of seawater [45]

$$\begin{cases} fv_g = g \frac{\partial \eta}{\partial x} \\ -fu_g = g \frac{\partial \eta}{\partial y} \end{cases} \quad (16)$$

where u_g and v_g are the zonal and meridional components of geostrophic current, respectively, x -axis points east, y -axis is northward. η is the sea surface dynamic height, which is the deviation of sea surface from geoid. Currently, both the sea surface height and geoid are generally determined by satellite geodetic techniques. The spatial resolution of sea surface height based on satellite altimetry data is about 20 – 30 km, and that of geoid based on satellite gravity field is about 100 – 150 km. The computational error in the geostrophic current due to measurement errors in sea surface height and geoid is about 5 – 20 cm/s on a spatial scale of 100 – 150 km [46], [47]. Due to the difficulty of obtaining a fine geostrophic current map that match the spatial resolution of the HF radar (2.5 km), this article approximates that the geostrophic currents are consistent throughout the experimental sea area.

Geostrophic currents can also be estimated from field measurements. The experimental sea area in this article is close to the west coast of the Taiwan Strait, whose coastline is oriented in a northeast–southwest direction. In order to facilitate the calculation of sea currents, the (x, y) coordinate system is rotated to (x_R, y_R) , where x_R -axis points in the offshore direction, y_R -axis is along the Chinese coastline and positive poleward. The (x_R, y_R) coordinate system is shown in Fig. 4. If the surface and bottom stresses are taken into account, the following sea current momentum equations can be obtained [48]:

$$fv_R = g \frac{\partial \eta}{\partial x_R} - \frac{\tau_R^x}{h} + \frac{\tau_R^{bx}}{h} \quad (17a)$$

$$-fu_R = g \frac{\partial \eta}{\partial y_R} - \frac{\tau_R^y}{h} + \frac{\tau_R^{by}}{h} \quad (17b)$$

where (u_R, v_R) is the depth-averaged current vector in the (x_R, y_R) coordinate system. (τ_R^x, τ_R^y) is the wind stress vector and $(\tau_R^{bx}, \tau_R^{by})$ is the kinematic bottom stress vector ($m^2 s^{-2}$).

The bottom stress can be parameterized as $\tau_R^{bx} = \sigma h u_R$, $\tau_R^{by} = \sigma h v_R$, where σ is a friction coefficient ($\sim 1.66 \times 10^{-5} s^{-1}$ [49]). In the near-coast regions, $v_R \gg u_R$, thus (17b) can be approximated as [48]

$$\sigma v_R = -g \frac{\partial \eta}{\partial y_R} + \frac{\tau_R^y}{h}. \quad (18)$$

In near-shore areas it is useful to write $\eta = \eta_0 + \eta'$, where η_0 denotes a slowly varying large-scale sea level which is externally imposed, and η' is a fluctuating part which depends on the sea current [50]. In the Taiwan Strait, the pressure gradient $g \partial \eta' / \partial y$ is small compared to $g \partial \eta_0 / \partial y$ due to the Kuroshio and/or warmer water of the South China sea [49]. In addition, the time scale over which η_0 changes (months and longer) is much longer than that for wind to change (a few days to 1–2 weeks) [49]. So the alongshore gradient $\partial \eta / \partial y$ can be considered to be stable compared to the wind. Therefore, it can be concluded from (18) that using measurements of alongshore wind speed and current velocity at different moments, it is possible to fit a relationship between them and derive the alongshore current velocity v_{R0} when the alongshore wind speed is zero. v_{R0} can be viewed as the geostrophic current since it depends only on the gradient $\partial \eta / \partial y_R$.

A large number of studies have been conducted to calculate the steady alongshore surface current in the Taiwan Strait, and they are close in value [51], [52], [53]. For example, it is suggested in Zhu et al.'s [52] work that this current is 0.1 m/s and pointing northeast, which is adopted in this article. Since the time scale for changes in the major component of the geostrophic current ($g \partial \eta_0 / (\sigma \partial y)$) is comparable to or larger than the duration of the experiment in this article (less than two months), it is assumed that the geostrophic currents are constant throughout the experimental period.

D. Design of LSTM Network

LSTM network is a typical recurrent neural network (RNN). Its main advantage lies in the ability to remember the past information for a long time, and at the same time, it can avoid the problems of gradient disappearance and gradient explosion that are prone to occur in the traditional RNN, which enables the network to better handle long sequential data. The sea surface current data dealt with in this article are long time series, and data at different moments are correlated. Hence LSTM network is adopted.

Fig. 3(a) shows the ARC speed varying with the significant wave height at the same location. The ARC speed is extracted from HF radar data and the wave height is measured by a buoy in the radar coverage. It can be seen that when wave height is low, the ARC is insensitive to the change in wave height, while when wave height is high, there is a strong correlation between the ARC and the wave height.

Fig. 3(b) shows a scatter plot of the intersection angle between ARC and wind direction relative to the wave height. The former

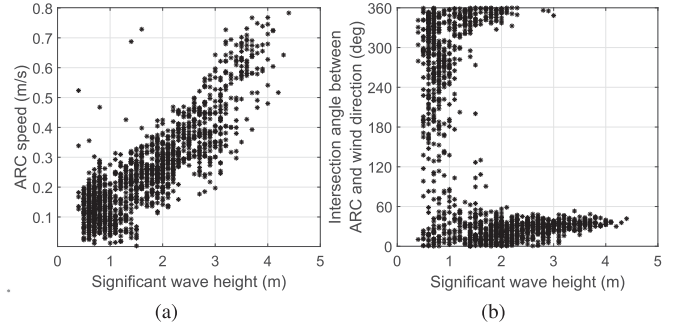


Fig. 3. (a) Radar-measured ARC speed versus buoy-measured significant wave height. (b) Intersection angle between radar-measured ARC and wind direction versus buoy-measured significant wave height.

is retrieved from HF radar data and the latter is provided by the buoy. The intersection angles are scattered over a wide area at low wave heights, but clustered over a narrow range at high wave heights.

Comparing Fig. 3(a) and (b) with Fig. 1(c) and (d), respectively, it can be seen that the trends of ARC speed and direction with wave height for the measured data are close to those of the numerical simulations, although not exactly the same in value. The measured angles between ARCs and wind directions at low wave heights are very different from the simulation results, largely due to the big error in wind direction measurements in this case caused by the unsteady airflow. In addition, at low wave heights, ARC is low in speed and thus is easily to fluctuate under the influence of the surrounding environment, which leads to the instability of its direction. At high wave heights, ARC is similar in direction to a theoretical Ekman current at the surface (45° to the right of the wind), indicating that the wind-induced current is the main component of ARC in this case.

The input variables for the cascaded network contain the zonal and meridional components of the ARC and the wind direction. It can be seen from Fig. 3(b) that although the intersection angle between ARC and wind direction does not highly correlate to the wave height, its distribution range does. Therefore, wind direction is also used as an input variable to the cascaded network.

Since the distribution characteristics of the ARC with respect to the wave height at high sea state are quite different from those at low sea state, using different inversion models for high and low sea states is beneficial to improve the inversion accuracy, which is why a cascade-structured network is adopted in this article. Based on the data characteristics shown in Fig. 3(a) and (b), wave heights below 1 m are defined as low sea state and those above 1 m are defined as high sea state.

The cascaded LSTM network can be divided into two stages. As Fig. 2 shows, the first stage is the sea state classification model, which divides the input data into two groups of high and low sea states. The second stage contains two models, one performing wave height inversion for low sea state data and one processing high sea state data. The final wave height maps are obtained by combining the wave height values from these two models.

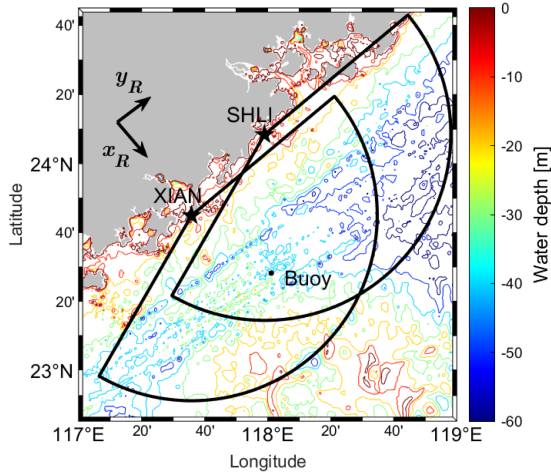


Fig. 4. Experimental map in Taiwan Strait. Two stars mark the radar sites (XIAN and SHLI) and one dot marks the buoy. The two black arrows indicate the coordinate system of (17) (cross-shore and alongshore).

TABLE I
HF RADAR PARAMETERS

Parameter	Value
Carrier frequency	13 MHz
Maximum detection range	100 km
Spatial resolution	2.5 km
Temporal resolution	0.5 h
Velocity resolution	0.03 m/s

IV. EXPERIMENTAL RESULTS AND DISCUSSION

A. Experiment Background

To verify the performance of the proposed method, experimental data obtained from February to March in 2013 on the western side of Taiwan Strait are used. As shown in Fig. 4, during the experiment, two HF radars were deployed in XIAN and SHLI, respectively, which are 60.5 km apart. The transmitting waveforms of both radars are FMICW, and the receiving antennas are compact monopole/cross-loop antennas. The two radars are capable of achieving 100 km of ocean surface current observations, whose coverage area are marked by the sectors in Fig. 4. The main operating parameters are given in Table I.

The ground truth data used to evaluate the algorithm performance come from two sources. One is a buoy deployed at a distance of 46 and 42 km from XIAN and SHLI, respectively, as shown in Fig. 4, which measures wave height, surface current, wind speed and direction every half hour. The other is the numerical wave height field provided by European Center for Medium-range Weather Forecasts (ECMWF) [54]. In order to spatially and temporally align with the radar wave height inversion results, the initial numerical wave field with a temporal resolution of 6 h and a spatial resolution of $0.125^\circ \times 0.125^\circ$ is linearly interpolated in three dimensions (time, latitude, longitude), resulting in a temporal resolution of 0.5 h and a spatial resolution of $0.025^\circ \times 0.025^\circ$. The correlation coefficient (CC) between the wave heights from the buoy and the numerical model at the buoy position is 0.98 and the mean square deviation is 0.21 m.

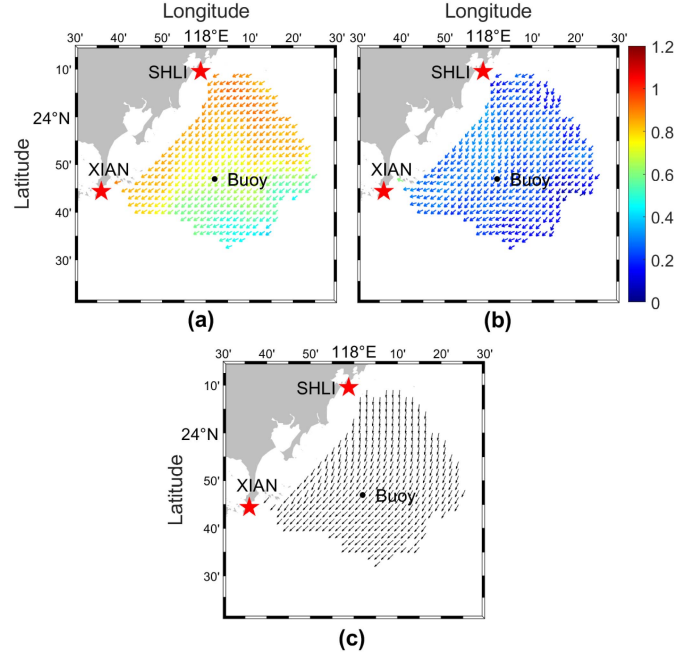


Fig. 5. Radar-measured (a) vector current map, (b) ARC map, and (c) wind direction map at 1:30 A. M. Feb. 11. The color bar denotes the current velocity in m/s.

TABLE II
SIGNIFICANT TIDAL CONSTITUENTS AT THE LOCATION OF THE BUOY

name	freq (cph)	vmax (m/s)	vmin (m/s)	phase($^\circ$)
M_2	0.0805	0.3865	0.0348	241.9523
S_2	0.0833	0.1399	0.0143	299.5432
MSF	0.0028	0.1157	0.0115	110.7377
N_2	0.0790	0.0544	0.0160	200.2176

B. ARC Map and Wind Direction Map

Fig. 5(a) shows a typical vector current map obtained during the experiment. The velocities range from 0.5 to 1 m/s and are slightly greater in areas near the coast than away from the coast. The directions are mainly southwest and parallel to the coastline. The vector currents measured by the radars at the location of the buoy are in good agreement with the buoy measurements. Using the buoy data as the ground truth, it is calculated that the root-mean-square error (RMSE) and CC are 0.091 m/s and 0.93 for current velocity and 28.4° and 0.94 for current direction, respectively [55].

Table II gives the four main tidal components obtained from harmonic analysis of the radar-measured currents at the location of the buoy, where freq means frequency in cycle per hour (cph), vmax is the maximum velocity, and vmin is the minimum velocity. It can be seen that the M_2 tidal component is the most significant constituent, which suggests that the tidal current here is predominantly semidiurnal.

Subtracting tidal and geostrophic currents from the vector currents gives the ARCs, as shown in Fig. 5(b). The velocities are between 0.1 and 0.5 m/s, which are significantly reduced compared to the vector current velocities. The directions are mostly southwest and nearly parallel to the coastline.

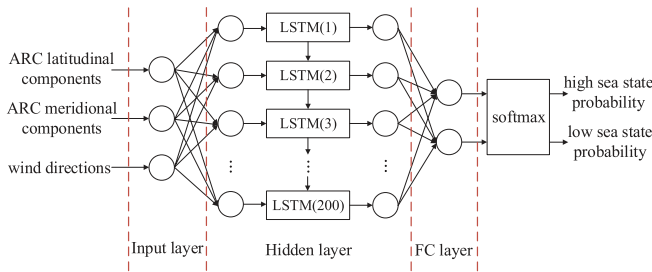


Fig. 6. Structure of LSTM sea state classification model.

Fig. 5(c) shows the radar-measured wind direction map at the same moment. The wind directions in the lower part of the map are close to the directions of ARCs in the same area. Using the ECMWF-provided numerical model as the ground truth, the RMSE of the radar's wind direction measurements is calculated as 45.4° . This error is larger than that documented in the existing literature [55], mainly because the former is the result of a large sea area comparison and the latter is the result of a single point comparison. As stated in Section III-D, it is the variation range of the angle between ARC and wind direction rather than the angle value itself that is utilized to estimate wave height, so the wind direction is still used as an input parameter despite its large error.

C. Result of Sea State Classification Model

Fig. 6 shows the structure of the LSTM sea state classification model, which includes an input layer, a hidden layer, a fully connected layer (FC layer), and a softmax classifier. The data entering the input layer include the two orthogonal components (latitudinal and meridional) of the ARCs and the wind directions. The hidden layer, which contains 200 LSTM neurons, maps the input data to high-dimensional feature space and learns the dependency relationships between the data based on their recurrent structures for feature extraction. The FC layer maps the high-dimensional features output by the hidden layer to the label space. The softmax classifier calculates the probability that the input data at each moment corresponds to a high sea state and the probability that it corresponds to a low sea state, respectively. Whichever of these two probabilities is greater than 0.5, the input data at this moment is classified into the corresponding sea state category, i.e., either the high sea state category or the low sea state category.

During the two-month experiment, a total of 2670 sets of data were acquired at a 0.5-h interval, of which the first 70% (1869 sets) are used for model training and the second 30% (801 sets) are used for testing. When training the model, the sea state categories obtained from the buoy-measured wave heights are used as the labels, the training epochs is 100, the batch size is 32, the initial learning rate is 0.001, and the Adam optimizer is used.

In order to evaluate the performance of LSTM sea state classification model, two other classification models based on backpropagation (BP) neural network and support vector machine (SVM), respectively, are used for comparison. These two models are trained using the same datasets as the LSTM model.

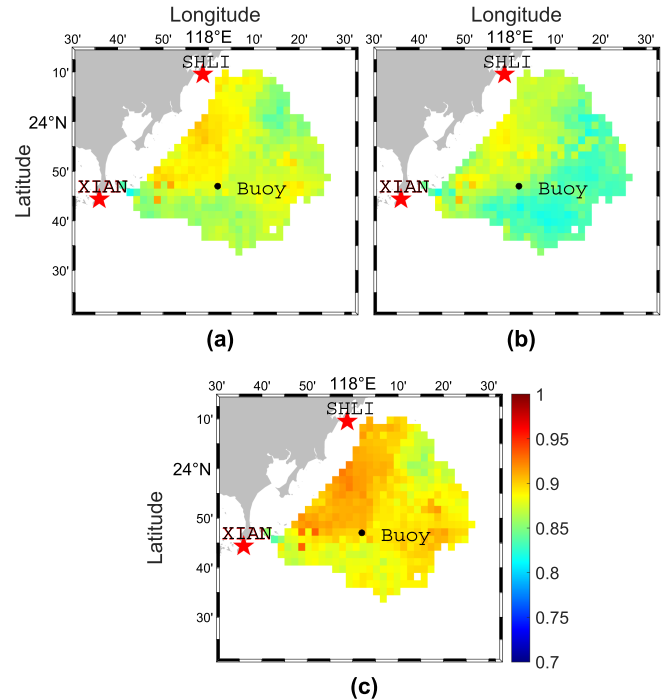


Fig. 7. Spatial distribution of accuracy for three sea state classification models. (a) BP model. (b) SVM model. (c) LSTM model. The color bars denote the classification accuracy.

Taking the sea state categories corresponding to the buoy measurements as the true categories, the classification accuracies in the grid where the buoy is located computed using the testing datasets are: BP—0.92, SVM—0.92, LSTM—0.96. All three models have over 0.9 accuracy, with the LSTM network having the highest. Accuracy is defined in this article as the ratio of the number of samples with correct category judgments to the total number of samples tested. In order to test the spatial generalization ability, the three models are applied to all spatial grid cells within the radar's coverage, and the outputs are compared with the sea state categories corresponding to the numerical wave fields. Fig. 7 shows the classification accuracies calculated using the testing datasets. Over a wide range of sea surface, the accuracies of all three models are above 0.8. The LSTM model has the highest accuracy, which can be attributed to the fact that the LSTM model better utilizes the temporal correlation of the input data.

D. Result of Wave Height Inversion Model

Based on the sea state category results, the ARC and wind direction data can be categorized into two groups: high and low sea states. The high sea state wave height inversion model and the low sea state wave height inversion model process these two groups of data, respectively. The final wave height inversion results are obtained by combining the outputs from these two models. The high sea state inversion model and the low sea state inversion model have the same structure, but since they are trained separately using different data, they have different model weights. Fig. 8 shows the structure of each LSTM wave height

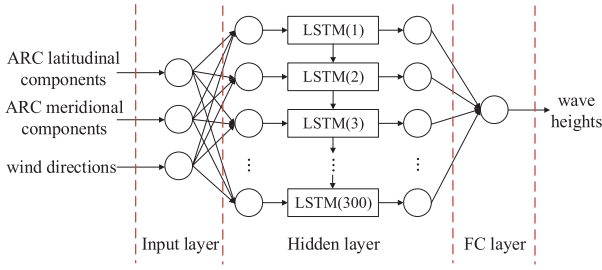


Fig. 8. Structure of LSTM wave height inversion model.

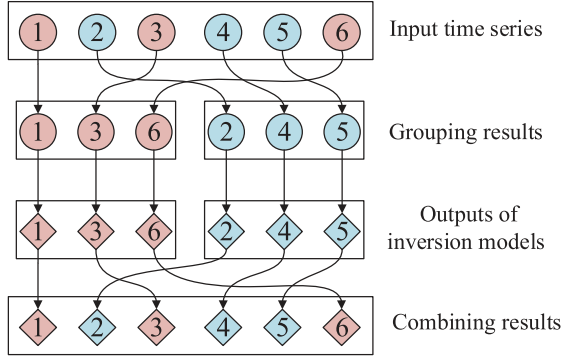


Fig. 9. Schematic diagram of grouping and combining data. Circles and diamonds in red indicate data that are categorized into the high sea state group and those in blue indicate data that are categorized into the low sea state group.

inversion model, which consists of an input layer, a hidden layer and an FC layer. The input layer inputs the categorized time series data, and the hidden layer, which contains 300 LSTM neurons, performs the feature extraction and learning. The FC layer is used to linearly transform the high-dimensional features output by the hidden layer into the network prediction results, i.e., the wave heights. Fig. 9 illustrates how the output data from the two inversion models are combined into the final wave height inversion results. In the input time series, the six datasets are numbered in chronological order. The input data are then categorized into two groups: high sea state and low sea state. The red circles indicate data that are treated as high sea state data and the blue circles indicate data that are considered to be low sea state data. The order of the datasets is changed after grouping, but the original moments corresponding to each dataset are additionally recorded. Two inversion models perform wave height inversion for these two groups, respectively, and the outputs of the models, which are represented by red and blue diamonds, are in the same order as the grouping results. Finally, the outputs of the two inversion models are rearranged in chronological order based on the original moments corresponding to each dataset recorded earlier.

Based on the buoy-measured wave heights, the 1869 training sets are divided into 1071 high sea state training sets and 798 low sea state training sets, and the 801 testing sets are divided into 465 high sea state testing sets and 336 low sea state testing sets. When training the wave height inversion models, the training epochs is 300, the batch size is 32, the initial learning rate is 0.001, and the Adam optimizer is adopted.

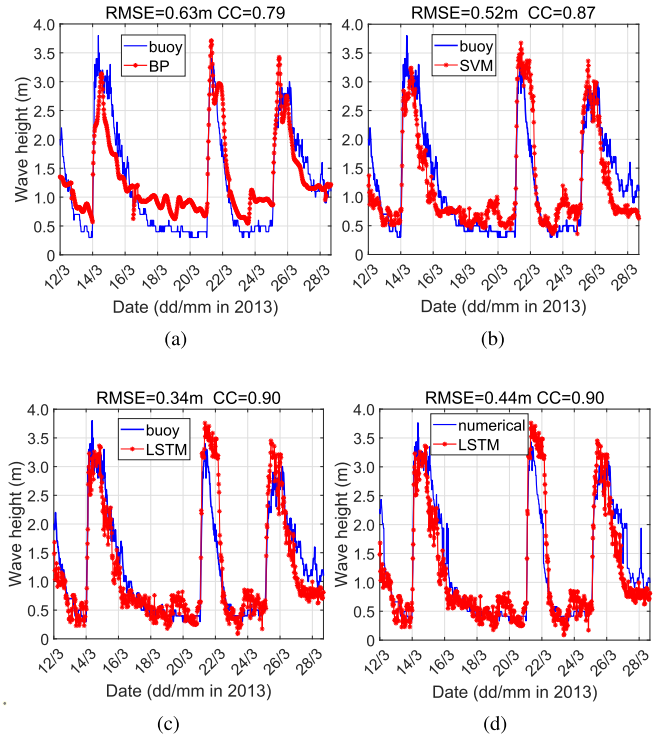


Fig. 10. Wave heights at the buoy's location. (a) BP models. (b) SVM models. (c) LSTM models. (d) LSTM models and numerical wave height field.

In order to evaluate the performance of LSTM-based wave height inversion models, wave height inversion models based on BP network and SVM are also designed for comparison.

Fig. 10 shows the wave heights at the location of the buoy retrieved from the testing datasets. Each plot is a combination of the outputs from the high sea state inversion model and the low sea state inversion model constructed using the same method. In Fig. 10(a)–(c), the buoy measurements are plotted as the ground truth data, and in Fig. 10(d), the ground truth data are the numerical wave height field outputs. The RMSE and CC corresponding to each plot are calculated. It can be seen that the LSTM models have the lowest error, especially in low sea state.

E. Result of Cascaded Model

As Fig. 2 shows, the cascaded model in this article refers to a model constructed by cascading a sea state classification model and two wave height inversion models. The sea state classification model and the wave height inversion models are trained separately. When training the two wave height inversion models for high and low sea states, the input data are classified according to the buoy-measured wave heights which are treated as the real wave heights in this article. That is, during the training phase, the wave height inversion models are not related to the sea state classification model. After the training is finished, they are cascaded to use, i.e., the input data of the wave height inversion models are classified according to the outputs of the sea state classification model.

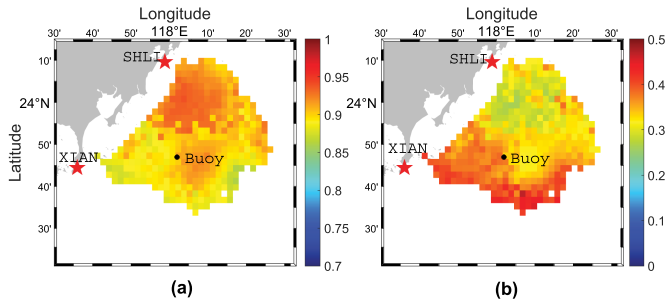


Fig. 11. Spatial distribution of wave height inversion errors for LSTM-LSTM model. (a) CC. (b) RMSE in m.

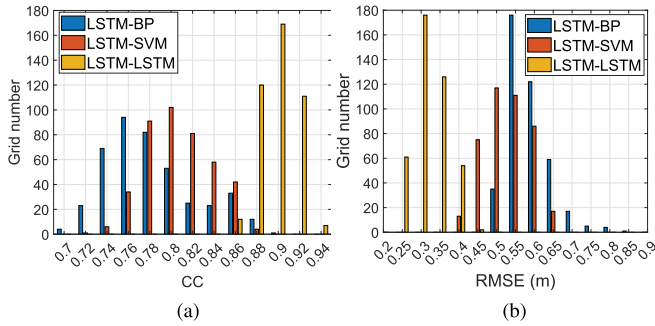


Fig. 12. Number of spatial grids with wave height inversion errors in different intervals. (a) CC. (b) RMSE.

The comparisons in Section IV-C illustrate that the LSTM-based sea state classification model has the highest accuracy and, therefore, the LSTM classification model is combined with the inversion models constructed by three methods, respectively, to form three cascaded models, LSTM-BP, LSTM-SVM, and LSTM-LSTM. Using the numerical wave height field as the ground truth, wave height inversion errors in different spatial grids in radar coverage can be calculated. Fig. 11(a) and (b) shows the CCs and RMSEs for LSTM-LSTM model computed using the testing datasets, respectively. CCs are basically distributed between 0.85 and 0.95, and RMSEs between 0.30 and 0.45 m. The spatial variability in error performance may be caused by the spatial differences in geostrophic currents. In the process of calculating the ARCs, the geostrophic currents are set to be the same throughout the experimental area, which is not realistic and will inevitably introduce an error into the inversion results. Although how large this error is cannot be estimated at this time due to the lack of ground truth data, the inversion results suggest that the effect of the geostrophic current errors on the wave height inversion is within the range of reception.

Fig. 12 gives the correlation and error histograms for the three cascaded networks LSTM-BP, LSTM-SVM, and LSTM-LSTM. In Fig. 12(a), the LSTM-LSTM network has the highest CC overall. The mean values of CCs for the three networks LSTM-BP, LSTM-SVM, and LSTM-LSTM are 0.79, 0.81, and 0.90, respectively. In Fig. 12(b), the average RMSEs for the three networks are 0.61, 0.55, and 0.35, respectively. In summary, LSTM-LSTM network has the best inversion accuracy and therefore serves as the final selected inversion network.

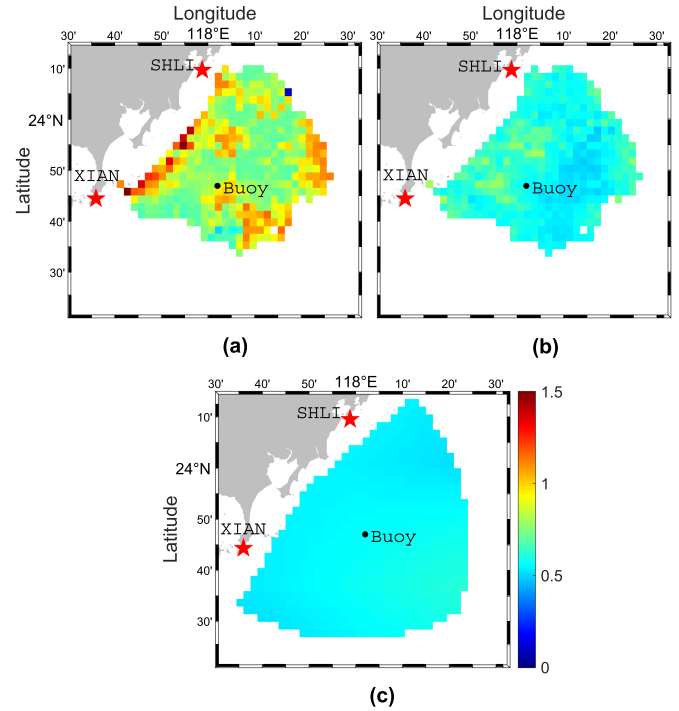


Fig. 13. Wave height maps measured in low sea state. (a) Noncascaded LSTM network. (b) Cascaded LSTM network. (c) Numerical wave height field. (The buoy-measured wave height is 0.6 m. The wave heights where the buoy is located in (a), (b), and (c) are 0.78, 0.55, and 0.58 m, respectively.)

F. Ablation Experiment

In order to verify the benefit of the cascade structure on the accuracy of wave height inversion, an ablation experiment is performed considering a noncascaded LSTM network without a sea state classification model. The input data to the noncascaded network are the ARCs and wind directions that have not been classified by sea state, and the output data are the wave height values. The training datasets and hyperparameters are kept consistent with the those of the cascaded LSTM network in Section IV-D. Fig. 13 shows the wave height maps obtained by the noncascaded and cascaded LSTM networks, respectively, in the low sea state case, as well as the numerical wave height field. The numerical wave heights range from 0.52 to 0.62 m with a mean value of 0.56 m. Wave heights calculated by the noncascaded network are significantly higher than the numerical wave height field, ranging from 0.10 to 1.54 m, with a mean value of 0.86 m. The cascaded network generated wave height ranges from 0.48 to 0.80 m, with an average value of 0.60 m, which is closer to the numerical wave height field than that of the noncascaded network.

Fig. 14 compares the inversion results of noncascaded and cascaded LSTM networks in the high sea state. The measurement mean values of the two networks are 2.08 and 2.13 m, respectively, with the latter being closer to the numerical wave height field with a mean value of 2.53 m.

From the above-mentioned comparison, it can be seen that the inversion accuracy of the cascade network is higher, especially in the low sea state. The reason is that the relationship between

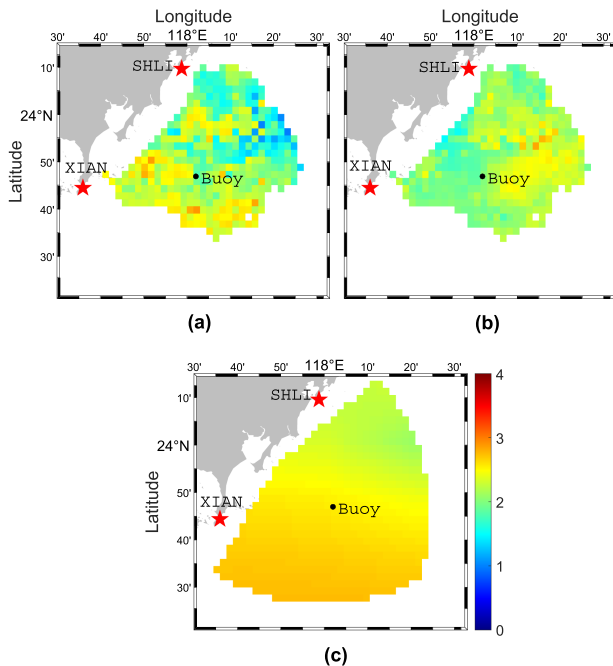


Fig. 14. Wave height maps measured in high sea state. (a) Noncascaded LSTM network. (b) Cascaded LSTM network. (c) Numerical wave height field. (The buoy-measured wave height is 2.3 m. The wave heights where the buoy is located in (a), (b), and (c) are 1.79, 2.03, and 2.52 m, respectively.).

wave height and ARC in the low sea state is different from that in the high sea state, so separating the low and high sea state data before inversion can greatly improve the inversion accuracy.

V. CONCLUSION

In this article, a wave height map inversion method using HF-radar measured surface currents and wind directions is proposed. Through theoretical analysis and numerical simulation, it is concluded that the sum of wind-induced current and wave-induced current is closely related to the wave height. This sum of currents, which is defined in this article as the ARC, can be obtained by removing the tidal and geostrophic currents from the vector current. According to the buoy-measured data, it is found that the ARC changes differently with wave height in high and low sea states, so a cascaded LSTM network is used for wave height inversion which is composed of two stages. The first stage divides the ARC and wind direction data into two groups, high sea state, and low sea state, and the second stage performs wave height inversion for each of the two groups. The final wave height maps are combinations of the inversion results of the two groups. By comparing with the numerical wave height field, the RMSE of the radar retrieved maps is calculated to be 0.35 m and the CC to be 0.90.

There are several papers that use other different wave height inversion methods for the same radar experimental data as in this article. Their results are described in the following for comparison with the method of this article.

It is difficult to obtain the wave height map using the algorithm based on the second-order continuum spectrum due to its low SNR, so the comparison experiment is performed only between

the inversion results of this algorithm at a distance of 10.5 km from XIAN station and the buoy measurements, which yields an RMSE of 0.6 m and a CC of 0.87 [55].

Using an algorithm based on the power ratio of the SHP to the Bragg peak, the wave height maps can be obtained, which have an RMSE of 0.33–0.77 m and a CC of 0.78–0.94 if the buoy measurements are taken as the ground truth data [19]. The accuracy of this algorithm in the center region of the radar coverage is close to that of the proposed algorithm in this article (RMSE 0.30–0.45 m, CC 0.85–0.95), but due to its sensitivity to the SNR of the SHP, it is less accurate in the border region and in low sea states.

The wave height inversion algorithm based on first-order peak power can also generate wave height maps, but at a radar frequency of 13 MHz, the sensitivity of first-order peak power to wave height is low, so this algorithm is not applicable [14].

In summary, the algorithm proposed in this article has comparable or better inversion accuracy than existing algorithms, and with fewer limitations on the spatial range and radar operating frequency. However, the experimental data processed in this article all correspond to wave heights lower than 5 m, so the inversion accuracy at higher sea state still needs to be examined.

As described in Section III-C, this article assumes that the geostrophic currents are the same throughout the experimental sea area and constant over the duration of the experiment. Due to the lack of the ground truth data of geostrophic currents, it is impossible to give the errors of the geostrophic currents in this article. However, the wave height inversion results show that the above-mentioned assumptions are reasonable. If the wave heights are to be inverted over a longer time span, the variation of the geostrophic currents with time cannot be neglected. Measurements of sea level anomalies from satellites or buoys can be used to correct the geostrophic current values. Alternatively, the cascaded LSTM network can be retrained using wave heights from buoy measurements or from other HF radar algorithms (e.g., second-order continuum spectrum-based algorithm) to compensate for wave height inversion errors due to changes in the geostrophic currents.

In the tidal current extraction of this article, the harmonic constants of each space cell are assumed to be invariant during the whole experiment, so the harmonic analysis is only done once for each space cell. However, if the tidal currents are to be calculated over a longer time span, such as one year, the change of harmonic constants over time should be considered and multiple harmonic analyses are required. The interval between two adjacent harmonic analyses can be set from a few days to a month.

Currently, this method has only been used on the western side of Taiwan Strait, and its performance in other sea areas needs to be tested. If the method is to be applied to other sea area, there are two problems that need to be solved. First, the geostrophic current information of this sea area must be known. Second, if swells are significant in this sea area, the relationship between ARC, wind direction and wave height will be more complicated than that in the experimental sea area in this article, which is dominated by wind waves, so the model needs to be retrained and possibly restructured if necessary.

REFERENCES

- [1] D. E. Barrick, "First-order theory and analysis of MF/HF/VHF scatter from the sea," *IEEE Trans. Antennas Propag.*, vol. AP-20, no. 1, pp. 2–10, Jan. 1972.
- [2] D. E. Barrick, "Remote sensing of sea state by radar," in *Remote Sensing of the Troposphere*, V. E. Derr, Ed. Washington, DC, USA: U.S. Government Printing Office, 1972, ch. 12, pp. 1–46.
- [3] D. E. Barrick, "Extraction of wave parameters from measured HF radar sea-echo Doppler spectra," *Radio Sci.*, vol. 12, no. 3, pp. 415–424, 1977.
- [4] M. L. Heron, P. Dexter, and B. McGann, "Parameters of the air-sea interface by high-frequency ground-wave Doppler radar," *Mar. Freshwater Res.*, vol. 36, pp. 655–670, 1985.
- [5] W. Huang, S. Wu, E. Gill, B. Wen, and J. Hou, "HF radar wave and wind measurement over the Eastern China Sea," *IEEE Trans. Geosci. Remote Sens.*, vol. 40, no. 9, pp. 1950–1955, Sep. 2002.
- [6] C. W. Evans, H. J. Roarty, J. T. Kohut, and S. M. Glenn, "Examination of the SeaSonde wave processing settings and the effects of shallow water on wave measurements," in *Proc. Oceans*, Hampton Roads, VA, USA, 2012, pp. 1–6.
- [7] D. E. Barrick, "The ocean waveheight nondirectional spectrum from inversion of the HF sea-echo Doppler spectrum," *Remote Sens. Environ.*, vol. 6, no. 3, pp. 201–227, 1977.
- [8] Y. Hisaki, "Nonlinear inversion of the integral equation to estimate ocean wave spectra from HF radar," *Radio Sci.*, vol. 31, no. 1, pp. 25–39, Jan. 1996.
- [9] N. Hashimoto, L. R. Wyatt, and S. Kojima, "Verification of a Bayesian method for estimating directional spectra from HF radar surface backscatter," *Coastal Eng. J.*, vol. 45, no. 2, pp. 255–274, 2003.
- [10] C. Zhao, M. Deng, Z. Chen, F. Ding, and W. Huang, "Ocean wave parameters and nondirectional spectrum measurements using multifrequency HF radar," *IEEE Trans. Geosci. Remote Sens.*, vol. 60, 2022, Art. no. 4204413.
- [11] B. Lipa and B. Nyden, "Directional wave information from the SeaSonde," *IEEE J. Ocean. Eng.*, vol. 30, no. 1, pp. 221–231, Jan. 2005.
- [12] L. R. Wyatt, J. J. Green, and A. Middleditch, "HF radar data quality requirements for wave measurement," *Coastal Eng.*, vol. 58, no. 4, pp. 327–336, 2011.
- [13] Z. Tian, B. Wen, L. Jin, and Y. Tian, "Radio frequency interference suppression algorithm in spatial domain for compact high-frequency radar," *IEEE Geosci. Remote Sens. Lett.*, vol. 15, no. 1, pp. 102–106, Jan. 2018.
- [14] H. Zhou and B. Wen, "Wave height extraction from the first-order Bragg peaks in high-frequency radars," *IEEE Geosci. Remote Sens. Lett.*, vol. 12, no. 11, pp. 2296–2300, Nov. 2015.
- [15] D. E. Barrick and B. J. Lipa, "Range angle determination with MUSIC direction finding," U.S. Patent 599083 4A, Nov. 23, 1999.
- [16] L. R. Wyatt, "Shortwave direction and spreading measured with HF radar," *J. Atmospheric Ocean. Technol.*, vol. 29, no. 2, pp. 286–299, 2012.
- [17] H. Zhou, H. Roarty, and B. Wen, "Wave height measurement in the Taiwan strait with a portable high frequency surface wave radar," *Acta Oceanologica Sinica*, vol. 34, no. 1, pp. 73–78, 2015.
- [18] L. Jin, B. Wen, and H. Zhou, "A new method of wave mapping with HF radar," *Int. J. Antennas Propag.*, vol. 2016, Aug. 2016, Art. no. 4135404.
- [19] Z. Tian et al., "Wave-height mapping from second-order harmonic peaks of wide-beam HF radar backscatter spectra," *IEEE Trans. Geosci. Remote Sens.*, vol. 58, no. 2, pp. 925–937, Feb. 2020.
- [20] Y. Tian, B. Wen, H. Zhou, C. Wang, J. Yang, and W. Huang, "Wave height estimation from first-order backscatter of a dual-frequency high frequency radar," *Remote Sens.*, vol. 9, no. 11, 2017, Art. no. 1186.
- [21] Y. Tian, Z. Tian, J. Zhao, B. Wen, and W. Huang, "Wave height field extraction from first-order Doppler spectra of a dual-frequency wide-beam high-frequency surface wave radar," *IEEE Trans. Geosci. Remote Sens.*, vol. 58, no. 2, pp. 1017–1029, Feb. 2020.
- [22] Y. Tian, Z. Tian, J. Zhao, and B. Wen, "Hybrid wave height estimation from first- and second-order doppler spectral peaks of compact high frequency radar," in *Proc. Glob. Oceans: Singapore-U.S. Gulf Coast*, 2020, pp. 1–4.
- [23] X. Zhang, X. Chu, and S. Wang, "Significant wave height inversion using the HF-SWR system based on EOS-ELM," *Periodical Ocean Univ. China*, vol. 49 (Sup. I), pp. 163–169, 2019.
- [24] B. Wen, W. Tang, and Y. Tian, "Significant wave height field inversion of high frequency radar based on BP neural network," *J. Huazhong Univ. Sci. Technol. (Natural Sci. Edition)*, vol. 49, no. 4, pp. 114–119, 2021.
- [25] F. Liu and H. Zhou, "Cross-domain submesoscale eddy detection neural network for HF radar," *Remote Sens.*, vol. 13, 2021, Art. no. 2441.
- [26] M. C. Tran, A. Sentchev, S. Berti, N. K. Ayoub, T. Nguyen-Duy, and N. K. Cuong, "Assessment of relative dispersion in the gulf of Tonkin using numerical modeling and HF radar observations of surface currents," *Continental Shelf Res.*, vol. 245, 2022, Art. no. 104784.
- [27] A. C. Martin, C. P. Gommenginger, B. Jacob, and J. Staneva, "First multi-year assessment of Sentinel-1 radial velocity products using HF radar currents in a coastal environment," *Remote Sens. Environ.*, vol. 268, 2022, Art. no. 112758.
- [28] C. Wen, Y. Tian, and B. Wen, "Wind speed extraction based on high frequency radar retrieved wind-driven current," *IEEE Geosci. Remote Sens. Lett.*, vol. 18, no. 9, pp. 1555–1559, Sep. 2021.
- [29] A. C. Ceres-Euse, A. Molcard, N. Bourg, D. Dumas, C.-A. Gurin, and G. Besio, "Breakdown of near-surface sea current from high-frequency radar data," *J. Atmospheric Ocean. Technol.*, vol. 39, no. 12, pp. 1927–1942, 2022.
- [30] V. Ekman, "On the influence of the Earth's rotation on ocean-currents," *Arkiv Matematik, Astronomi och fysik, Almqvist & Wiksells boktryckeri, A.-B.*, Band 2, no. 11, 1905.
- [31] M. Yelland and P. K. Taylor, "Wind stress measurements from the open ocean," *J. Phys. Oceanogr.*, vol. 26, no. 4, pp. 541–558, 1996.
- [32] P. E. Dexter and S. Theodoridis, "Surface wind speed extraction from HF sky wave radar Doppler spectra," *Radio Sci.*, vol. 17, no. 3, pp. 643–652, 1982.
- [33] J. Röhrs et al., "Surface currents in operational oceanography: Key applications, mechanisms, and methods," *J. Oper. Oceanogr.*, vol. 16, no. 1, pp. 60–88, 2023.
- [34] K. E. Kenyon, "Stokes drift for random gravity waves," *J. Geophysical Res. (1896-1977)*, vol. 74, no. 28, pp. 6991–6994, 1969.
- [35] I. Langmuir, "Surface motion of water induced by wind," *Science*, vol. 87, no. 2250, pp. 119–123, 1938.
- [36] A. J. Bowen, "Rip currents: 1. Theoretical investigations," *J. Geophysical Res. (1896-1977)*, vol. 74, no. 23, pp. 5467–5478, 1969.
- [37] R. H. Stewart and J. W. Joy, "HF radio measurements of surface currents," *Deep Sea Res. Oceanographic Abstr.*, vol. 21, no. 12, pp. 1039–1049, 1974.
- [38] O. S. Madsen, "A realistic model of the wind-induced Ekman boundary layer," *J. Phys. Oceanogr.*, vol. 7, no. 2, pp. 248–255, 1977.
- [39] K. F. Hasselmann et al., "Measurements of wind-wave growth and swell decay during the joint north sea wave project (JONSWAP)," in *Proc. Ergänzungsheft zur Deutschen Hydrographischen Zeitschrift Reihe A*, 1973, pp. 1–95.
- [40] M. S. Longuet-Higgins, D. E. Cartwright, and N. D. Smith, "Observations of the directional spectrum of sea waves using the motions of a floating buoy," in *Ocean Wave Spectra*. Englewood Cliffs, NJ, USA: Prentice-Hall, Inc., 1961, pp. 111–132.
- [41] H. Mitsuyasu et al., "Observations of the directional spectrum of ocean waves using a cloverleaf buoy," *J. Phys. Oceanogr.*, vol. 5, no. 4, pp. 750–760, 1975.
- [42] M. A. Donelan, J. Hamilton, and W. H. Hui, "Directional spectra of wind-generated waves," *Philos. Trans. Roy. Soc. London A: Math., Phys. Eng. Sci.*, vol. 315, no. 1534, pp. 509–562, 1985.
- [43] Y. Lai, H. Zhou, and B. Wen, "Surface current characteristics in the Taiwan strait observed by high-frequency radars," *IEEE J. Ocean. Eng.*, vol. 42, no. 2, pp. 449–457, Apr. 2017.
- [44] R. Pawlowicz, B. Beardsley, and S. Lentz, "Classical tidal harmonic analysis including error estimates in MATLAB using TIDE," *Comput. Geosci.*, vol. 28, no. 8, pp. 929–937, 2002.
- [45] Z. Hui and Y. Xu, "The impact of wave-induced Coriolis-Stokes forcing on satellite-derived ocean surface currents," *J. Geophysical Res.: Oceans*, vol. 121, no. 1, pp. 410–426, 2016.
- [46] X. Bai, H. Yan, Y. Zhu, P. Peng, and Y. Shen, "Progress in mean dynamic topography and geostrophic current research based on satellite geodetic techniques," *Prog. Geophys.*, vol. 31, no. 5, pp. 2063–2071, 2016.
- [47] W. Sui et al., "The construction of high precision geostrophic currents based on new gravity models of GOCE and satellite altimetry data," *Acta Oceanologica Sinica*, vol. 40, no. 3, pp. 142–152, 2021.
- [48] E. Liao, L. Y. Oey, X.-H. Yan, L. Li, and Y. Jiang, "The deflection of the China coastal current over the Taiwan Bank in winter," *J. Phys. Oceanogr.*, vol. 48, no. 7, pp. 1433–1450, 2018.
- [49] L. Y. Oey, Y. L. Chang, Y. C. Lin, M. C. Chang, S. Varlamov, and Y. Miyazawa, "Cross flows in the Taiwan Strait in winter," *J. Phys. Oceanogr.*, vol. 44, no. 3, pp. 801–817, 2014.
- [50] G. T. Csanady, *Circulation in the Coastal Ocean*. Berlin, Germany: Springer, 1982.

- [51] S. Wang, "Statistical characteristics of residual current and wind in western Taiwan Strait," *J. Oceanogr. Taiwan Strait*, vol. 10, no. 2, pp. 105–109, 1991.
- [52] D. Zhu, L. Li, Y. Li, and X. Guo, "Seasonal variation of surface currents in the southwestern Taiwan Strait observed with HF radar," *Chin. Sci. Bull.*, vol. 53, no. 15, pp. 2385–2391, 2008.
- [53] Z. Hu et al., "Characterizing surface circulation in the Taiwan Strait during NE monsoon from geostationary ocean color imager," *Remote Sens. Environ.*, vol. 221, pp. 687–694, 2019.
- [54] D. P. Dee et al., "The ERA-Interim reanalysis: Configuration and performance of the data assimilation system," *Quart. J. Roy. Meteorological Soc.*, vol. 137, no. 656, pp. 553–597, 2011.
- [55] C. Wang et al., "Validation and intercomparison of sea state parameter estimation with multisensors for OSMAR-S high-frequency radar," *IEEE Trans. Instrum. Meas.*, vol. 69, no. 10, pp. 7552–7565, Oct. 2020.



Yingwei Tian (Member, IEEE) was born in Qianjiang, Hubei, China, in 1989. He received the B.Eng. degree in communication engineering and the Ph.D. degree in communication and information systems from Wuhan University, Wuhan, China, in 2010 and 2015, respectively.

From 2015 to 2018, he was a Postdoctoral Fellow in geophysics with Wuhan University, where he is currently an Associate Professor. From 2018 to 2019, he was a Visiting Scholar with Memorial University, St. Johns, NL, Canada. His research interests include

the hardware design and signal processing of HF and UHF radar systems, and their application to the ocean surface remote sensing.



Jing Yang (Member, IEEE) was born in Xiangyang, Hubei, China, in 1983. She received the B.E. degree in electronic information science and technology and the Ph.D. degree in communication and information systems from Wuhan University, Wuhan, China, in 2005 and 2010, respectively.

Since 2011, she has been with the School of Electronic Information, Wuhan University. Her research interests include ocean surface remote sensing and signal processing.



Caijun Wang received the B.S. degree in radio physics, the M.S. degree in circuit and system, and the Ph.D. degree in signal processing from Wuhan University, Wuhan, China, in 2003, 2005, and 2008, respectively.

Since 2008, he has been with the Radar and Signal Processing Lab, Electronic Information School, Wuhan University. In August 2016, he was a Visiting Scholar with the Memorial University of Newfoundland, St. Johns, NL, Canada. His research interests include radio frequency system design, test,

and verification, ocean and river surface parameters remote sensing via high-frequency/ultrahigh-frequency radar, and radar data processing and applications.



Xinyi Ma was born in Hubei, China, in 2000. She received the B.Eng. degree in communication engineering from Wuhan University, Wuhan, China, in 2018, where she is currently working toward the master's degree in information and communication engineering.

Her research interests include vessel targets detection and tracking for high-frequency ground wave radar.



Xuqing Yan was born in Shanxi, China, in 1999. She received the B.Eng. degree in communication engineering from Central South University, Changsha, China, in 2021, and the M.Eng. degree in electronic information from Wuhan University, Wuhan, China, in 2023.

Her research focuses on wave height field inversion using high-frequency ground wave radar.